Computational Materials Science 117 (2016) 380–389

Contents lists available at ScienceDirect

Computational Materials Science

journal homepage: www.elsevier.com/locate/commatsci

The electronic and magnetic properties of anion doped (C, N, S) $GaFeO_3$; an *ab initio* DFT study

J. Atanelov *, P. Mohn

Institute of Applied Physics, Vienna University of Technology, Gußhausstraße 25-25a, 1040 Vienna, Austria

ARTICLE INFO

Article history:
Received 23 November 2015
Received in revised form 4 February 2016
Accepted 10 February 2016
Available online 27 February 2016

Keywords:
Multiferroics
Magnetism
Anion doping
Superexchange
Photocatalysis

ABSTRACT

In this study we present *ab initio* DFT calculations performed on stoichiometric and anion doped $GaFeO_3$ substituting O by a C, N and S atom, respectively. Stoichiometric $GaFeO_3$ has an antiferromagnetic (AFM) ground state. The Fe atoms of the sublattices Fe1 and Fe2 couple antiferromagnetically via the O atoms through the superexchange mechanism. Replacing the superexchange mediating O atom with p-elements of a different valence electron configuration changes the underlying magnetic exchange mechanism and influence the ground state properties. This may be used for tuning properties interesting for technical applications. Four different doping configurations were examined revealing a cell site dependent influence on the magnetic properties. Carbon, for example, changes the AFM coupling present in the Fe1–O–Fe2 configuration into a ferrimagnetic exchange for the Fe1–C–Fe2 bond. Depending on the respective cell site C substitution introduces a ferrimagnetic or AFM ground state. Nitrogen alters the ground state magnetic moment as well and sulfur introduces large structural distortions affecting the band gap and the overall AFM coupling inside the doped $GaFeO_3$ simulation cell. We give a detailed discussion on the respective magnetic exchange mechanisms and electronic properties with regard to applications as photocatalysis and use the predictive power of *ab initio* DFT simulations that may trigger future experiments in the very promising field of tunable multifunctional devices.

1. Introduction

Multiferroics like $GaFeO_3$ (GFO) are promising materials for a broad field of applications and have attracted great attention during the last years [1–3]. Multifunctionalities combined in a single phase are very attractive for further development of sensors, spintronics and data storage devices.

Stoichiometric GFO is antiferromagnetic (AFM) and shows ferroelectric behavior in its ground state [4–6]. The AFM ground state originates from the AFM superexchange mediated via the Fe–O–Fe bonds inside the crystal. However, some applications, like data storage devices, demand a ferromagnetic (FM) behavior. Tailoring and controlling the magnetic properties of GFO can therefore be crucial.

A great number of experimental and computational studies discuss the effect of varying iron concentration on the magnetic properties. Increasing the amount of Fe atoms increases the net magnetic moment [4,7–10]. Adding additional Fe atoms creates unsaturated Fe–O–Fe bonds and leads to the observed ferrimagnetic ground state.

A multitude of studies investigate the effect of cation doping in multiferroics like $BiFeO_3$, ZnO and GFO to name but a few [11,12]. They report changes in the ground state properties which may be important for tailoring materials regarding new technical applications. Theoretical and experimental studies on Cr, Mn and Co doped GFO report changes of the structural parameters, the magnetic ground state and the Curie temperature depending on the respective substitution cite (Fe or Ga sites) [13–15].

A much smaller number of studies examine the effect of anion substitution, exchanging the O atom by another main group element. Nitrogen and fluorine doped $BiFeO_3$ and ZnO show changes in their ground state properties and report enhanced ferromagnetism, polarization and absorption shifts into the visible region [16,17].

There is an experimental study performed by Dhanasekaran and Gupta [19] investigating the effect of N and S doping on the photocatalytic properties of GFO substituting O. Transition metal oxides and their occurrence as multiferroics have proven to be good photocatalysts [18]. Dhanasekaran and Gupta [19] report a significant increase of the photocatalytic property producing H_2 by water splitting substituting O sites with N and S atoms, respectively. Water splitting using solar-radiation is a most promising way for producing sustainable fuel.

* Corresponding author.
E-mail address: ja@cms.tuwien.ac.at (J. Atanelov).

http://dx.doi.org/10.1016/j.commatsci.2016.02.017
0927-0256/

In this paper we present *ab initio* calculations performed on a pure and single anion doped GFO simulation cell. Based on our earlier investigation [20] we have chosen four O substitutional sites (see Fig. 1) exchanging O by a C, N and S atom, respectively.

We focus on a detailed discussion on the magnetic exchange mechanism present in the respective anion doped Fe–X–Fe (X = C, N, S) complex and its effect on ground state properties like the band gap and the total magnetic moment of the GFOX simulation cell.

Beside trying to explain the enhanced photocatalytic property reported by Dhanasekaran and Gupta [19] we use *ab initio* calculations as a predictive tool revealing properties that are useful for new applications and may help to interpret future experimental results.

2. Computational details and methods

All calculations were carried out with the *Vienna Ab initio Simulation Package* (VASP) [21–26]. The potential between the electrons and ionic cores is described with projector augmented wave (PAW) pseudopotentials [27].

The simulations were carried out on an 8 f.u. GFO unit cell containing 40 atoms. To provide a reliable description of the effects of electronic correlation the calculations were performed using the generalized gradient approximation in the Dudarev formalism [28], denoted as GGA + U, and Heyd–Scuseria–Ernzerhof (HSE) hybrid functionals [29–32]. Applying Dudarev's approach the effective on site coulomb- and exchange parameters U and J do not enter separately, but in the form of $U_{eff} = U—J$. Setting $U_{eff} = 4$ eV yields reliable results for the magnetic moments and the cell parameters as compared to experiment [20].

In the case of anion doped GFO the simulation cell was relaxed within the GGA + U approximation until all force components were smaller than 0.01 eV/Å. The atomic positions, the shape and the volume of the simulation cell was allowed to change during relaxation. Plane waves with an energy up to 550 eV were included in the basis set in order to avoid Pulay forces. The Brillouin-Zone integration was performed on a $6 \times 6 \times 6$ Γ centered k-mesh with a Gaussian smearing of 0.05 eV. Total energies were converged better than 1×10^{-6} eV.

We performed on top HSE calculations on the GGA + U relaxed cell geometries. HSE functionals are known to yield reliable results for the gap size and even more relevant the position of the impurity bands inside the gap which are of great importance regarding the photocatalytic properties [33–35].

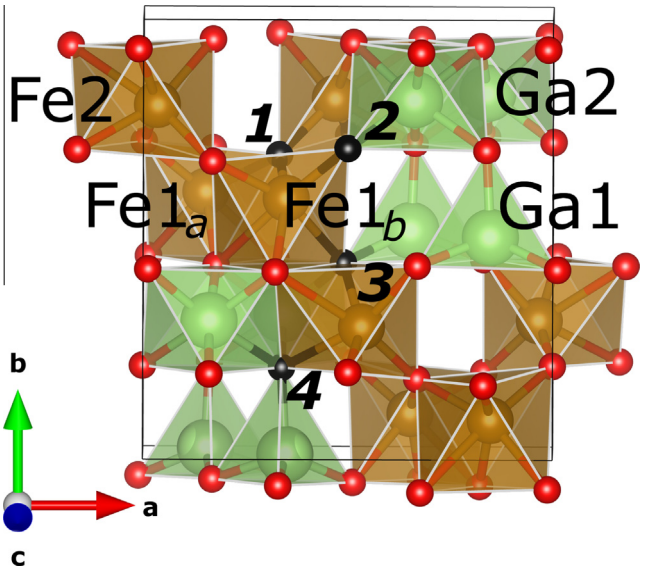

Fig. 1. Cell structure of stoichiometric GFO. The Ga1, Ga2, Fe1 and Fe2 sublattices are indicated as well as the four investigated doping sites (1)–(4).

For the HSE functional the short range/long range splitting parameter was set to $\omega = 0.7$ yielding an optimal description of the experimental band gap and crystal parameters [20]. Accounting for the vastly increased computation time the k-space integration was performed on a smaller $4 \times 4 \times 4$ Γ centered k-mesh.

To quantify the AFM superexchange of the investigated systems we introduce the AFM coupling strength as a main parameter. In stoichiometric GFO the AFM coupling strength is defined as the energy difference between the AFM ground state and a hypothetical FM state. Forcing the system into a FM state breaks the ground state AFM couplings. The corresponding energy difference is taken as a reference to measure the AFM coupling strength. Introducing anion dopants to the GFO simulation cell can create a magnetic ground state with a total magnetic moment unequal to zero. The AFM coupling strength is then defined by the energy difference between the actual magnetic ground state of the anion doped systems and a hypothetical FM state.

To gain better insight in the magnetic exchange mechanism, we partly integrated the density of states of the investigated systems. To some extent the thereby computed occupation numbers depend on the chosen muffin tin radii (O = 1.55 Å, C = 1.63 Å, N = 1.40 Å, S = 2.2 Å). Hence, the integrated O p and Fe d states have to be taken with caution and can not immediately be compared to oxidation numbers.

3. Stoichiometric GFO

Stoichiometric GFO has a noncentrosymmetric crystal structure and belongs to the $Pc2_1n$ (No. 33) space group. Its unit cell is orthorhombic with experimentally determined lattice parameters of $a = 8.735$ Å, $b = 9.383$ Å, and $c = 5.077$ Å [36]. Formally Fe and Ga are both in a 3^+ state, whereas oxygen is in a 2^- state. GFO has four cationic sublattices (Ga1, Ga2, Fe1 and Fe2) (Fig. 1). The Fe1 and Fe2 atoms are as well as the Ga2 sites surrounded each by an oxygen octahedron. The Ga1 atoms are located inside oxygen tetrahedra.

The Ga and the O atoms are both non magnetic, whereas the Fe atoms exhibit a magnetic moment of about $4\mu_B$ per atom [4,36,37]. In a fully ionic picture Fe is in a 3^+ state and left with 5 valence electrons in its $3d$-shell. This would result in a magnetic moment of $5\mu_B$. Measurements and calculations, however, show a local magnetic moment of about $4\mu_B$. In a previous study [20] we give a detailed discussion on the "virtual electron transfer" mechanism resulting in the observed $4\mu_B$ per Fe atom. The magnetic moments of the Fe1 and Fe2 atoms couple antiferromagnetically through the magnetic superexchange turning GFO into an AFM semiconductor. The AFM superexchange is mediated via the Fe1–O–Fe2 bonds throughout the crystal introducing a layer like magnetic ordering.

Fig. 2 shows the projected density of states (PDOS) of the $Fe1_a$–O(1)–Fe2 complex inside stoichiometric GFO. Visible are the equal magnetic moments of the $Fe1_a$ and Fe2 d-states given in red and yellow, respectively. The O p-states, highlighted in blue, are mainly populated in the energy range of −5 eV up to −1 eV. Taking a closer look at the $Fe1_a$ d-states one recognizes populated states in the spin up channel. In addition to the 5 electrons occupying the spin down channel we find an extra electron in the spin up channel. This additional electron originates from the "virtual electron transfer" and leads to the observed about $4\mu_B$ per Fe atom [20]. Same is true for the Fe2 atom.

In stoichiometric GFO the AFM superexchange is dominated by two Fe1–O–Fe2 complexes. These are the $Fe1_a$–O(1)–Fe2 and $Fe1_b$–O(2)–Fe2 configuration with an enclosed angle of 126.34° and 123.01°, respectively (see Fig. 1). For visualizing the latter the simulation cell has to be replicated in c direction. Geometrically

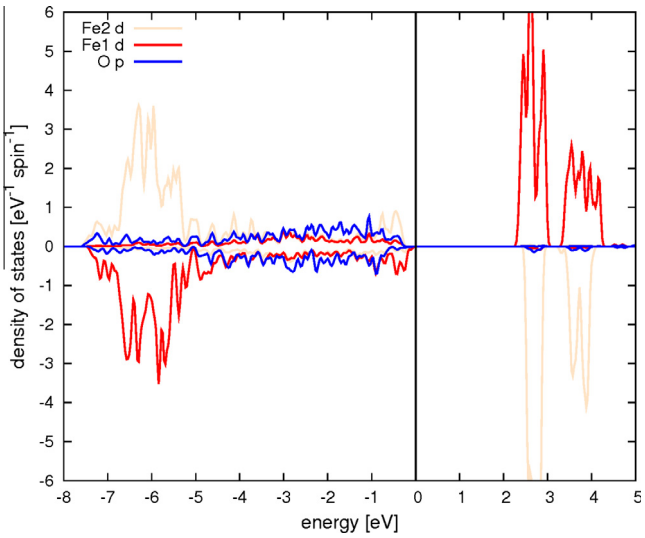

Fig. 2. PDOS of the Fe1$_a$–O(1)–Fe2 configuration in stoichiometric GFO. Given in red and beige are the Fe1$_a$ and Fe2 *d*-states. Highlighted in blue are the O *p*-states. (For interpretation of the references to color in this figure legend, the reader is referred to the web version of this article.)

these two complexes are connected to each other forming an Fe1–O–Fe2 twisted chain. Stoichiometric GFO contains two Fe1–O–Fe2 chains formed by the four upper left and four lower right Fe atoms (Fig. 1). The Fe1$_b$–O(3)–Fe2 complex connecting these two chains shows a reduced AFM coupling. A detailed list of the AFM coupling strengths of the corresponding Fe1–O–Fe2 configurations is given in Atanelov and Mohn [20].

Oxygen plays a crucial role in the AFM superexchange mechanism. Exchanging the O atom by another nonmetal X = C, N, S could affect and alter the magnetic exchange inside the respective doped Fe1–X–Fe2 complex and as a consequence change the electronic and magnetic properties of the GFO host matrix. Since there are two Fe1–O–Fe2 complexes dominating the AFM superexchange the respective cell site occupation may be substantial for the resulting magnetic coupling and ground state magnetic moment.

Fig. 1 shows the four substitutional O sites, highlighted in black. Site (1) and (2) are both part of the AFM coupling strength dominating Fe1–O–Fe2 complexes. Lattice site (3) connects the Fe1$_b$ atom of the upper chain to an Fe2 atom of the lower magnetic chain forming the Fe1$_b$–X(3)–Fe2 configuration that is characterized by a weak bonding in stoichiometric GFO. The next nearest neighbors of cell site (4) are a Ga and an Fe2 atom. In undoped GFO the corresponding Fe2–O(4)–Ga configuration shows no magnetic coupling since the Ga atom is non magnetic.

Anion doping can affect the GFO simulation cell in several ways. Beside local alterations of the magnetic exchange mechanism changes in the cell geometry are introduced as well which again influence the magnetic coupling.

We compared properties like the band gap, the total magnetic moment per simulation cell and the magnetic moment of the impurity atoms and the surrounding Fe atoms as well as cell structure parameters for all doping configurations with each other. Structural parameters of interest are the Fe1–X–Fe2 (X = C, N, O, S) bond length and enclosed angle of the corresponding substitution site. The corresponding parameters of the stoichiometric GFO simulation cell are given in Table 1. The Fe1–O and Fe2–O distances are almost equal showing only small variations. The respective O atoms are essentially non magnetic and the Fe atoms carry an absolute magnetic moment of about 4.1 μ_B (see Table 1). The band gap calculated within the HSE approximation is 2.68 eV for the spin up and 2.65 eV for the spin down gap. The calculated

Table 1
Geometric, magnetic and electronic properties of the respective cell sites (1)–(4) in stoichiometric GFO. The simulation cell was relaxed using the GGA + U approximation followed by an on top HSE calculation.

X=	O(1)	O(2)	O(3)	O(4)
Cell volume (Å^3)	416.17	416.17	416.17	416.17
Fe1$_a$–X (Å)	1.96	–	–	–
Fe1$_b$–X (Å)	1.97	1.93	2.09	–
Fe2–X (Å)	1.89	1.94	2.09	2.13
Fe1$_a$–X–Fe2 (°)	126.34	–	–	–
Fe1$_b$–X–Fe2 (°)	123.01	123.01	102.62	–
M_{tot} (μ_B)	0	0	0	0
X (μ_B)	−0.07	−0.02	+0.003	+0.07
Fe1$_a$ (μ_B)	−4.10	−4.10	−4.10	−4.10
Fe1$_b$ (μ_B)	−4.10	−4.10	−4.10	−4.10
Fe2 (μ_B)	+4.09	+4.09	+4.09	+4.09
Band gap direct up|down (eV)	2.68|2.65	2.68|2.65	2.68|2.65	2.68|2.65
E$_{diff}$[AFM–FM] (eV)	−1.54	−1.54	−1.54	−1.54

AFM coupling strength is 1.54 eV. All energy differences (E$_{diff}$[AFM–FM]) given in this work are calculated per unit cell.

Fig. 3(a) and (b) shows the magnetization density (spin up minus spin down) of the Fe1$_a$–O(1)–Fe2 complex inside the stoichiometric GFO simulation cell. Given in red and blue are the positive and negative magnetization densities, respectively. (a) Plots the spin density of all occupied states. Visible are the negative and positive spin densities of the Fe1$_b$ and Fe2 atom, respectively. The O(1) *p*-states are polarized, showing an inner and outer polarization. The inner polarization is more pronounced and has reversed orientation compared to the outer one which is decreased.

The outer polarization of the O(1) *p*-states can be more clearly seen in Fig. 3(b). They form an orbital overlap between the Fe atom and the O atom. This overlap corresponds to the virtual electron transfer and induces the AFM superexchange. Fig. 3(b) shows the partial spin density for the energy range of −5 eV up to the Fermi level and allows a better presentation of the superexchange mechanism.

The O *p*-states are almost evenly distributed over an energy range of −4 eV up to −1 eV (see Fig. 2).

Regarding the PDOS of the anion doped systems (see the following sections), there is an increased number of electronic states near the Fermi level. This most likely can be attributed to an enhanced interaction with the neighboring Fe atoms and to the reduced electronegativity of the anion dopants. The magnetic exchange mechanism in these systems is located in the upper part of the PDOS between −1 eV up to the Fermi level. The following anion doped partial magnetization densities are therefore plotted in this respective energy range.

Plotting the partial magnetization density for stoichiometric GFO in the range of −1 eV up to the Fermi level would yield equal spatial spin density distributions as shown in Fig. 3(b) but with vastly decreased intensities. The superexchange mechanism and its overlapping Fe–O orbitals are therefore much less visible anymore.

Hence, comparing the partial magnetization densities of pure and anion doped GFO is still reasonable for the chosen energy ranges.

Noteworthy we do not include inner cationic site disorder to our calculations keeping the system simple in a first approach. Inner cationic side disorder describes site changes of Ga and Fe atoms which are well known for GFO and often seen in experiment [4,10,36,38].

4. Anion doped GFO

4.1. Carbon doping

Substituting a single O atom with a C atom has various effects on the GFO host matrix. It increases the cell volume and can

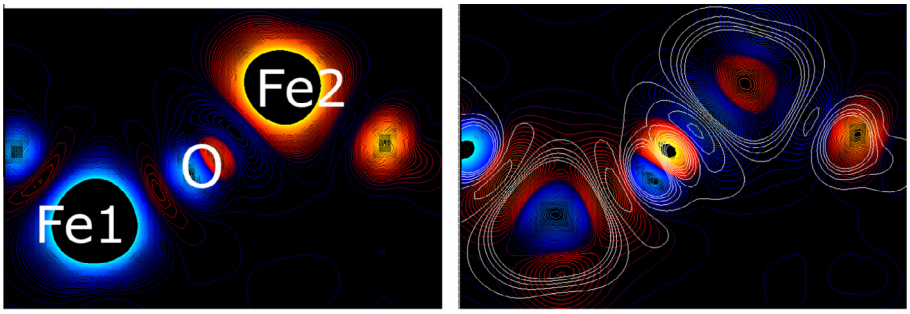

Fig. 3. Magnetization density of the $Fe1_a$–O(1)–Fe2 complex inside stoichiometric GFO. Given in red and blue are positive and negative spin densities, respectively. (a) Shows the spin density of all occupied states. (b) Gives the partial spin density in the energy range of −5 eV up to the Fermi level. A coarse mesh of the total magnetization density shown in (a) is overlaid (highlighted in white) to illustrate the spatial extent of the covalent bond. (For interpretation of the references to color in this figure legend, the reader is referred to the web version of this article.)

introduce a net magnetic moment to the GFO host matrix (see Table 2). The C(1) substitution is the energetically most stable doping configuration. Substituting cell site (2) is only 4 meV less probable compared to the C(1) substitution and placing the C atom on site (3) is by 235 meV less favorable in energy. The cell site (4) substitution is the most unfavorable doping configuration with 507 meV energy difference compared to the C(1) case.

4.1.1. C(1) substitution

In the following we focus on the geometric, electronic and magnetic properties of C(1) doped GFO (GFOC(1)).

Starting with the structural properties of the $Fe1_a$–C(1)–Fe2 complex the $Fe1_a$–C(1) and Fe2–C(1) bonds show increased bond lengths variations compared to the $Fe1_a$–O(1)–Fe2 configuration in stoichiometric GFO (see Tables 1 and 2). The $Fe1_a$–C(1) bond is increased to 2.15 Å the Fe2–C(1) distance is reduced to 1.70 Å compared to undoped GFO. The overall $Fe1_a$–*X*(1)–Fe2 bond length, however, almost remains the same. Exchanging O with C increases the $Fe1_a$–*X*(1)–Fe2 enclosed angle from 126.34° to 131.99° and reduces the $Fe1_b$–*X*(1)–Fe2 enclosed angle from 123.01° to 121.14°.

In stoichiometric GFO each Fe atom carries a magnetic moment of about $4\mu_B$. In the C(1) substitution case, however, the Fe2 atom next to the C(1) atom has a reduced magnetic moment of about $+3\mu_B$ changing the actual AFM coupling into a ferrimagnetic exchange.

Fig. 4 shows the PDOS of the $Fe1_a$–C(1)–Fe2 complex inside GFOC(1) calculated within the HSE approximation. To gain better insight in the exchange mechanism the number of electrons are integrated dividing the PDOS into two parts. First includes the energy range of −8 eV up to −1 eV and second from −1 eV up to the Fermi level.

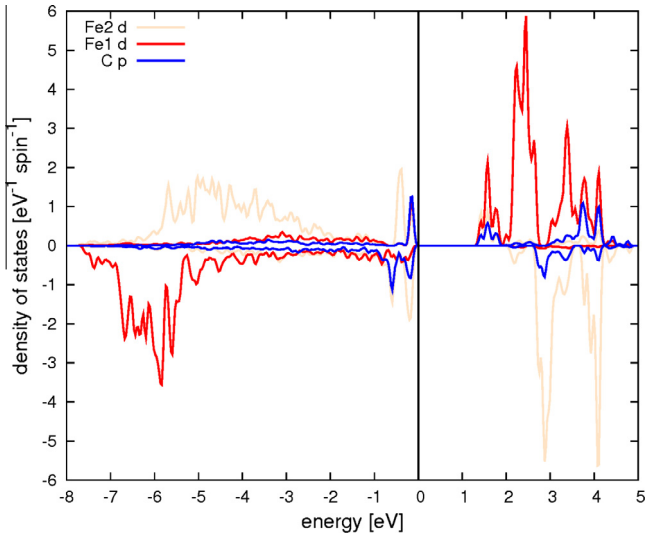

Fig. 4. PDOS of the $Fe1_a$–C(1)–Fe2 configuration in GFOC(1). Given in red and beige are the $Fe1_a$ and Fe2 *d*-states. Highlighted in blue are the C *p*-states. (For interpretation of the references to color in this figure legend, the reader is referred to the web version of this article.)

The PDOS of the $Fe1_a$ *d*-electrons in GFOC(1) and stoichiometric GFO are very similar (see Figs. 2 and 4). The magnetic exchange mechanism present between the $Fe1_a$–C(1) and the $Fe1_a$–O(1)

Table 2
Geometric, magnetic and electronic properties of single carbon doped GFO, regarding the doping configurations (1) to (4). The simulation cell was relaxed using the GGA + U approximation followed by an on top HSE calculation.

X=	C(1)	C(2)	C(3)	C(4)
Cell volume (Å^3)	432.37 (+3.9%)	433.64 (+4.2%)	431.94 (+3.8%)	433.56 (+4.2%)
$Fe1_a$–X (Å)	2.15 (+9.7%)	–	–	–
$Fe1_b$–X (Å)	2.17 (+10.2%)	2.14 (+10.9%)	2.01 (−4.0%)	–
Fe2–X (Å)	1.70 (−10.1%)	1.77 (−8.8%)	2.07 (−1.0%)	1.99 (−6.6%)
$Fe1_a$–X–Fe2 (°)	131.99 (+4.5%)	–	–	–
$Fe1_b$–X–Fe2 (°)	121.14 (−1.5%)	125.23 (+1.8%)	99.79 (−2.8%)	–
M_{tot} (μ_B)	−2	−2	0	−2
X (μ_B)	−0.42	−0.49	−0.03	−0.57
$Fe1_a$ (μ_B)	−4.10	−4.11	−4.10	−4.10
$Fe1_b$ (μ_B)	−4.10	−4.03	−3.72	−4.10
Fe2 (μ_B)	+2.88	+3.23	+3.78	+3.72
Band gap direct up|down (eV)	1.52|2.23	1.76|2.13	1.40|1.36	1.42|2.38
E_{diff}[AFM–FM] (eV)	−1.19	−1.39	−1.15	−1.33

atoms are therefore alike. Integrating the $Fe1_a$ *d*-states between −8 eV up to −1 eV yields 4.61 electrons in the spin down channel and another 0.72 electrons in the spin up channel. Adding the occupied states from −1 eV up to the Fermi level gives another 0.22 electrons in the spin down and 0.15 in the spin up channel, respectively yielding a total of 0.37 electrons. In sum there are about 5 electrons in the minority spin channel and another electron in the majority spin channel resulting in the observed $-4\mu_B$.

The Fe2 *d*-states on the other hand are shifted towards the fermi energy compared to stoichiometric GFO. Integrating the Fe2 *d*-states from −8 eV up to −1 eV gives 3.99 electrons in the spin up channel and another 0.92 electrons occupying the spin down channel yielding a magnetic moment of about $+3\mu_B$. Summing up the electronic states from −1 eV up to the Fermi level gives 0.413 electrons in the spin up and 0.632 electrons in the spin down channel adding up to 1.05 electrons.

Both the $Fe1_a$ and the Fe2 atom carry about 6 *d*-electrons each. The Fe2 atom, however, shows an accumulation of *d*-states near the Fermi level indicating an enhanced interaction with the C(1) atom.

Integrating the C *p*-states in the energy range of −8 eV to −1 eV gives 0.45 electrons in the spin down channel and another 0.33 electrons in the spin up channel. Adding up the electronic states from −1 eV up to the Fermi level yields a total of 0.56 *p*-electrons with 0.40 electrons occupying the minority spin channel and another 0.16 electrons in the majority spin channel. The C(1) anion has a magnetic moment of $-0.42\mu_B$ and carries 1.33 *p*-electrons.

The enhanced interaction and hybridization of Fe2 *d* and C(1) *p*-states near the Fermi level is favoured by the reduced Fe2–C(1) bond length. An Fe2 *d*-electron therefore becomes shifted upwards the fermi energy forming an additional covalent bond with the C(1) atom. The magnetic moment of the in energy shifted Fe2 *d*-electron, however, becomes compensated in that respective bond reducing the magnetic moment of the Fe2 atom to about $+3\mu_B$ introducing a ferrimagnetic coupling inside the $Fe1_a$–C(1)–Fe2 complex.

Adding up all magnetic contributions of the C(1) and Fe atoms, considering that the O atom show a small polarization as well, yields in a net magnetic moment of $-2\mu_B$ per simulation cell.

Fig. 5(a) and (b) shows spin density plots (spin up minus spin down) of the $Fe1_a$–C(1)–Fe2 complex with an enclosed angle of 131.99°. Given in red and blue are the positive and negative magnetization densities, respectively. Both (a) and (b) show an in-plane picture perpendicular to the *z*-axis. (a) Shows the spin density plot of the total DOS. Clearly visible are the positive and negative magnetization densities located at the $Fe1_a$ and the Fe2 atom respectively. The C(1) atom is polarized. The negative polarization is turned towards the Fe2 atom and the smaller positive magnetization faces the $Fe1_a$ atom. (b) Shows the partial magnetization density of the energy range of −1 eV up to the Fermi level. It reveals the spatial extent of the covalent bond formed within the $Fe1_a$–C(1)–Fe2 complex. A coarse mesh of the total magnetization density shown in (a) is overlaid (highlighted in white) to illustrate the spatial extent of the covalent bond. Clearly visible is the orbital overlap of the negative magnetization density given in blue between the C(1) and Fe2 atom. This overlap reduces the original $+4\mu_B$ of the Fe2 atom to the calculated $+3\mu_B$. The positive magnetization density overlap of the C(1) and the $Fe1_a$ atom on the other hand is less pronounced.

4.1.2. C(2) substitution

Introducing a C impurity at cell site (2) also introduces a total magnetic moment of $-2\mu_B$ per simulation cell and evokes a ferrimagnetic coupling inside the $Fe1_b$–C(2)–Fe2 configuration. The $Fe1_b$–*X*(2)–Fe2 enclosed angle is increased by +1.8% to 125.23°. The C(2)–$Fe1_b$ and C(2)–Fe2 bond lengths again vary while the first one is elongated and the second one reduced due to the enhanced covalent exchange interaction between the C(2) and Fe2 atom. Both the C(1) and C(2) substitutions induce a ferrimagnetic ground state and reduce the band gap compared to stoichiometric GFO. The respective band gaps are not symmetric due to the magnetic ground state.

4.1.3. C(3) substitution

Whereas cell site (1) and (2) are part of the AFM coupling mediating Fe1–O–Fe2 chains, cell site (3) and (4) are not. In stoichiometric GFO the O(3) atom mediates a very weak AFM coupling between its next nearest $Fe1_b$ and Fe2 atoms [20]. The respective $Fe1_b$ and Fe2 atoms are already "saturated" and do not enter further AFM superexchange interactions with additional O atoms outside these chains. Substituting cell site (3) with a C atom yields a non magnetic ground state. The C(3) impurity is non magnetic and the $Fe1_b$ and the Fe2 atoms show an absolute magnetic moment of about $4\mu_B$, each. The $Fe1_b$–C(3) and C(3)–Fe2 bond lengths vary marginally and are similar to the corresponding bonds in stoichiometric GFO. However, there is a small reduction of the magnetic moment of the $Fe1_b$ and Fe2 atom (see Table 2) suggesting the presence of a small orbital overlap and a weak interaction with the C(3) atom. Substituting cell site (3) with a C impurity reduces the band gap the most.

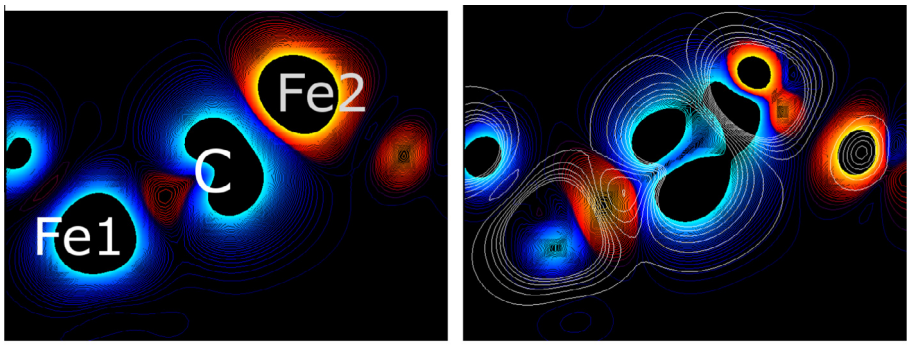

Fig. 5. Magnetization density of the $Fe1_a$–C(1)–Fe2 complex in GFOC(1). Given in red and blue are positive and negative spin densities, respectively. (a) Shows the spin density of all occupied states. (b) Gives the partial spin density in the energy range of −1 eV up to the Fermi level. (For interpretation of the references to color in this figure legend, the reader is referred to the web version of this article.)

4.1.4. C(4) substitution

The energetically most unfavorable doping configuration is the substitution of cell site (4). The next nearest cations are a Ga2 and Fe2 atoms. No Fe1–C(4)–Fe2 complex is formed in that particular case. However, the simulation cell shows a total magnetic moment of $-2\mu_B$. The Fe2–C(4) distance is reduced compared to the undoped Fe2–O(4) configuration. The cell volume is increased and the C(4) atom carries a magnetic moment of $-0.57\mu_B$. To rule out having found a meta stable solution a comparative calculation was performed forcing the simulation cell into a non magnetic ground state. The magnetic solution however remains more favorable by about 200 meV. Regarding Table 2 the next nearest Fe2 atom shows a reduced magnetic moment indicating an orbital overlap with the C(4) atom.

Surprisingly the C(3) and C(4) substitutions show different magnetic behavior. The non magnetic state of the C(3) atom can be attributed to its neighboring $Fe1_b$ and Fe2 atom. The distances to both Fe cations, which are part of the $Fe1_b$–C(3)–Fe2 complex, are almost symmetric. No strong covalent bond is formed as in the C(1) and C(2) substitution. The magnetic polarization introduced by the Fe neighbors fully compensates at the C(3) site ending up in a non magnetic state. In the C(4) substitution case the anion interacts only with its next nearest Fe2 cation. The C(4)–Fe2 distance is reduced compared to stoichiometric GFO and the C anion polarizes asymmetric with a finite magnetic moment.

4.2. Nitrogen doping

Substituting O with N leads to a ground state magnetic moment of $-1\mu_B$ per simulation cell for all investigated doping configurations. In any of the studied cases the N atom shows increased interaction with its next nearest Fe2 atom. The respective Fe2–N distances are reduced compared to the corresponding Fe2–O bonds in stoichiometric GFO. The decreased Fe2–N bond length introduces a larger orbital overlap between the N and the Fe2 atom. The magnetic moment of the Fe2 atom is slightly reduced by this overlap, especially notable for the N(3) and N(4) substitution sites (see Table 3). Introducing a N impurity enhances the cell volume and reduces the band gap for all doping configurations. The N(1) substitution is the energetically most stable doping configuration similar to the C(1) substitution. Almost equal in energy is the N (3) lattice site substitution with only 6 meV energy difference. Followed by that is the N(4) doping configuration being 43 meV less favorable. The energetically least probable N doping case is the N (2) lattice site occupation, with 70 meV energy difference compared to the N(1) configuration. The overall energy differences, however, are very small compared to the C substitutions.

4.2.1. N(1) substitution

Regarding the structural properties of the $Fe1_a$–N(1)–Fe2 complex, the $Fe1_a$–N(1) bond length is decreased and the N(1)–Fe2 bond increased by −1.6% and +4.1% respectively compared to stoichiometric GFO. Both Fe–O bonds experience less geometric alterations compared to the C(1) doped case. The $Fe1_a$–N(1)–Fe2 enclosed angle is enhanced by +1.1% to 127.75°. The cell volume is increased and the ground state shows a magnetic moment of $-1\mu_B$ per simulation cell, which could be expected since one hole is introduced substituting O by N.

Fig. 6 shows the PDOS of the $Fe1_a$–N(1)–Fe2 configuration (calculated within the HSE approximation). Given in beige and red are the Fe2 and $Fe1_a$ *d*-states, respectively. Highlighted in blue are the N(1) *p*-states. The DOS of the $Fe1_a$ and Fe2 *d*-states is similar to the undoped $Fe1_a$–O(1)–Fe2 configuration in stoichiometric GFO shown in Fig. 2. The Fe2 *d*-states are not shifted towards the Fermi level like in the C(1) doped case and the N(1) impurity introduces an acceptor state located near the center of the band gap.

There is an enhanced accumulation of N(1) *p*-states near the fermi energy similar to the C(1) doped case. The covalent bonding between the N(1) and Fe2 atom, however, is not as strong as in the C(1) substitution case. No additional covalent bond is formed reducing the magnetic moment of the corresponding Fe2 atom. Integrating the number of N(1) *p*-states in the energy range of

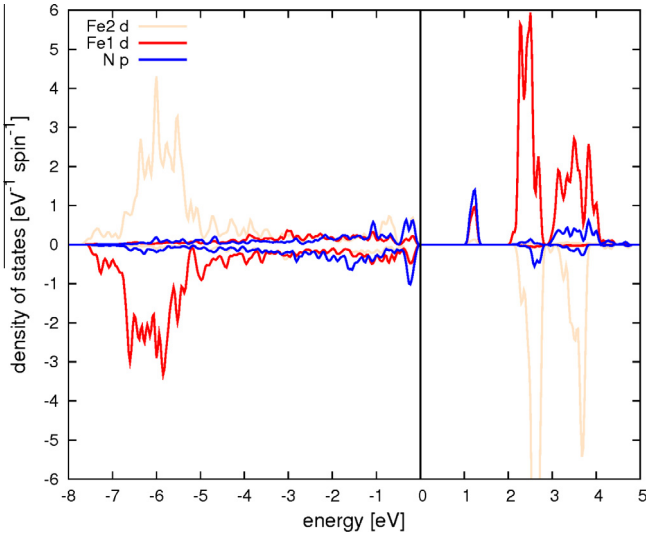

Fig. 6. PDOS of the $Fe1_a$–N(1)–Fe2 configuration in GFON(1). Given in red and beige are the $Fe1_a$ and Fe2 *d*-states. Highlighted in blue are the N *p*-states. (For interpretation of the references to color in this figure legend, the reader is referred to the web version of this article.)

Table 3
Geometric, magnetic and electronic properties of single nitrogen doped GFO, regarding the doping configurations (1) to (4). The simulation cell was relaxed using the GGA + U approximation followed by an on top HSE calculation.

X=	N(1)	N(2)	N(3)	N(4)
Cell volume (Å^3)	432.80(+4.0%)	432.84(+4.0%)	429.90(+3.3%)	429.70(+3.3%)
$Fe1_a$–X (Å)	2.04(+4.1%)	–	–	–
$Fe1_b$–X (Å)	2.05(+4.1%)	2.03(+5.2%)	2.07(−1.0%)	–
Fe2–X (Å)	1.86(−1.6%)	1.91(−1.5%)	1.94(−7.2%)	1.96(−8.0%)
$Fe1_a$–X–Fe2 (°)	127.75(+1.1%)	–	–	–
$Fe1_b$–X–Fe2 (°)	119.75(−2.7%)	122.83(−0.1%)	102.47(−0.1%)	–
M_{tot} (μ_B)	−1	−1	−1	−1
X (μ_B)	−0.61	−0.57	−0.29	−0.24
$Fe1_a$ (μ_B)	−4.06	−4.11	−4.11	−4.11
$Fe1_b$ (μ_B)	−4.05	−4.06	−4.07	−4.10
Fe2 (μ_B)	+3.97	+4.00	+3.66	+3.68
Band gap direct up|down (eV)	1.38|2.36	1.26|2.53	1.19|1.91	1.14|2.23
E_{diff}[AFM–FM] (eV)	−1.58	−1.45	−1.28	−1.39

−1 eV up to the Fermi level gives a total of 0.51 electrons. The respective electrons are almost evenly distributed among both spin channels. 1.81 N *p*-states are occupied in the energy range of −8 eV up to −1 eV yielding a magnetic moment of $-0.55\mu_B$. The N atom has a total of 2.31 *p*-electrons and a magnetic moment of about $0.61\mu_B$.

While 42% of the C(1) *p*-states are located in the small energy range of −1 eV up to the Fermi level only 22% of the N(1) *p*-electrons are found in the respective energy range. The N(1) *p*-states are therefore mainly located in lower energy ranges compared to the C(1) *p*-electrons. This can be attributed to the higher electronegativity of the N atom as well as to the weak N(1)–Fe2 covalent bond. The enhanced C(1)–Fe2 interaction shifts both the C(1) *p*-states and Fe2 *d*-states towards the Fermi level. The number Fe2 *d*-states in the energy range of −1 eV up to the Fermi level therefore gives information on the interaction with the respective anion dopant. In the C(1) doped case 1.05 Fe2 *d*-electrons are located in the corresponding energy range, whereas there are only 0.50 Fe2 *d*-electrons in the N(1) substitution case. The over all number of Fe2 *d*-electrons, though, differs negligible with 5.95 and 5.71 Fe2 *d*-electrons in the N(1) and C(1) doped case, respectively. The number of the $Fe1_a$ *d*-electrons are similar as well with 5.69 and 5.72 in the N(1) and C(1) substitution case.

Fig. 7(a) shows the total magnetization density and (b) the partial spin density for the energy range of −1 eV up to the Fermi level. All values are calculated within the HSE approximation. The negative magnetic density of the N(1) atom is peanut like shaped and has a small droplet formed positive magnetization density next to it. The positive magnetization density is more pronounced in the C(1) substitution, which can be attributed to the decreased magnetic moment of the C(1) impurity.

Fig. 7(b) shows the magnetic interaction present within the $Fe1_a$–N(1)–Fe2 complex. The interaction mediated via the N(1) atom is similar to the undoped $Fe1_a$–O(1)–Fe2 complex in stoichiometric GFO (see Fig. 3). Both show an inner and outer polarization of the anion *p*-states. The orbital overlap between the O(1) and the Fe states, however, is more pronounced.

The magnetization density of the energy range of −2 eV up to −1 eV (not shown here) is similar to the one shown in (a). The electrons forming the covalent bond are therefore solely located in the energy range of −1 eV up to the Fermi level.

4.2.2. N(2) substitution

The $Fe1_b$–N(2)–Fe2 complex shows larger differences in the single bond lengths and a slightly reduced magnetic moment of the N (2) atom. Cell volume and band gap are similar to the N(1) doped case. The enclosed angle is reduced by only 0.1% compared to stoichiometric GFO.

4.2.3. N(3) substitution

In the N(3) substitution case the respective the Fe2–N(3) bond experiences larger structural distortions compared to the N(1) and N(2) doping cases. The Fe2–N(3) distance becomes reduced by −7.2% and the $Fe1_b$–N(3) distance decreased by −1.0% compared to stoichiometric GFO. The enclosed angle however reduces by small −0.1%. The magnetic moments of the Fe2 and N(3) atom are decreased, compared to the N(1) and N(2) doping configurations. Spin up and spin down gap are reduced the most in this doping case.

4.2.4. N(4) substitution

In the N(4) substitution the next nearest cationic neighbors of the N(4) atom are a Ga2 and an Fe2 atom. The respective Fe2–N (4) distance is reduced by −8.0%. This is the largest Fe–N bond length reduction of all N doping cases. The magnetic moment of the Fe2 and N(4) atoms are reduced to $+3.68\mu_B$ and $-0.24\mu_B$, respectively.

4.3. Sulfur doping

Sulfur and oxygen have the same number of valence *p*-electrons. The S atom shows no magnetic moment in any of the investigated doping configurations leaving the ground state AFM. Incorporating a S atom introduces considerable lattice distortions due to the larger atomic radius and as a consequence influences the AFM coupling inside the crystal.

The S(1) doping configuration is the energetically most favorable substitution site. Followed by that is the S(2) substitution which is about 140 meV less probable. S(3) is the most unfavorable doping configuration with more than half an eV energy difference compared to the S(1) substitution. Placing the S atom on cell site (4) is about 450 meV less favorable in energy.

The magnetic coupling mediated via the S atom is similar to the one transferred by the O atom. A comparison of the AFM coupling strength of both systems is therefore reasonable. N and C on the other hand induce different magnetic coupling mechanisms such that a comparison of the AFM coupling strength with pure GFO is not meaningful (see Table 4).

4.3.1. S(1) substitution

Substituting O(1) with a S atom increases the cell volume by 6.4%. The $Fe1_a$–S(1) and the Fe2–S(1) bond lengths are elongated

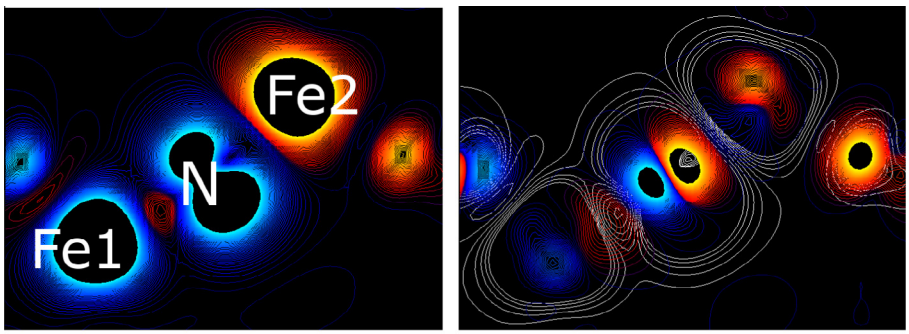

Fig. 7. Magnetization density of the $Fe1_a$–N(1)–Fe2 complex in GFON(1). Given in red and blue are positive and negative spin densities, respectively. (a) Shows the spin density of all occupied states. (b) Gives the partial spin density in the energy range of −1 eV up to the Fermi level. (For interpretation of the references to color in this figure legend, the reader is referred to the web version of this article.)

Table 4
Geometric, magnetic and electronic properties of single sulfur doped GFO, regarding the doping configurations (1) to (4). The simulation cell was relaxed using the GGA + U approximation followed by an on top HSE calculation.

X=	S(1)	S(2)	S(3)	S(4)
Cell volume (Å^3)	443.01(+6.4%)	443.09(+6.5%)	446.07(+7.2%)	445.19(+7.0%)
Fe1$_a$–X (Å)	2.29(+16.8%)	–	–	–
Fe1$_b$–X (Å)	2.31(+17.3%)	2.27(+17.6%)	2.31(+10.5%)	–
Fe2–X (Å)	2.24(+18.5%)	2.24(+15.5%)	2.31(+10.5%)	2.35(+10.3%)
Fe1$_a$–X–Fe2 (°)	130.17(+3.0%)	–	–	–
Fe1$_b$–X–Fe2 (°)	121.07(−1.6%)	119.35(−3.0%)	106.40(+3.7%)	–
M_{tot} (μ_B)	0	0	0	0
X (μ_B)	−0.09	+0.02	+0.03	+0.08
Fe1$_a$ (μ_B)	−4.02	−4.09	−4.13	−4.12
Fe1$_b$ (μ_B)	−4.01	−4.02	−4.01	−4.12
Fe2 (μ_B)	+4.01	+3.98	+4.01	+4.02
Band gap direct up|down (eV)	1.81|1.87	1.77|1.85	2.07|2.16	2.03|2.58
E_{diff}[AFM–FM] (eV)	−1.48	−1.45	−0.44	−1.51

by notable 16.8% and 18.5% respectively compared to stoichiometric GFO. This is in contrast to the C(1) and N(1) anion doping cases where the Fe2–X(1) distance is decreased introducing an enhanced interaction. The enclosed angle of the Fe1$_a$–S(1)–Fe2 configuration is increased to 130.17° and the band gap becomes reduced by more than 1 eV for each spin channel. S has the smallest electronegativity of all investigated anion dopants. A large part of the electronic *p*-states are therefore found in the upper part of the DOS in the energy range of −1 eV up to the Fermi level (see Fig. 8). Integrating the number of S *p*-electrons in the energy range of −8 eV up to the Fermi level gives 2.47 occupied states. 1.35 of these states are located between −8 eV and −1 eV. The remaining 1.13 electrons, which represent 46% of the S *p*-electrons, are found in the small energy of range of −1 eV up to the Fermi level. Both the Fe1$_a$ and the Fe2 atom carry 6 *d*-electrons and show an absolute magnetic moment of about 4μ_B.

Fig. 9(a) shows the total magnetization density of the respective Fe1$_a$–S(1)–Fe2 complex in GFOS(1). The inner and outer polarization show a decreased spin density compared to the Fe1$_a$–O(1)–Fe2 configuration in stoichiometric GFO (see Fig. 3(a)).

Fig. 9(b) shows the magnetization density within the energy range of −1 eV up to the Fermi level. The outer polarization presents the covalent bonding and shows decreased intensity compared to the inner polarization. Regarding the energy range of −4 eV up −1 eV (not shown here) the inner polarization vanishes and the outer antiparallel spin density expands over the inner one. Hence, a spatially expanded positive and negative magnetization density cloud remains at the S(1) site next to the Fe1 and Fe2 atom, respectively. The covalent bond between the S and Fe atoms is therefore mainly formed in the energy range of −4 eV up to −1 eV. The accumulation of S *p*-states near the Fermi level (see Fig. 9(b)) shows reduced interaction with the neighboring Fe atoms and mostly forms the inner polarization.

Plotting the whole energy range shown in Fig. 9(a), gives a superimposed picture of the discussed partial energy ranges. These compensate each other adding up to a reduced total spin polarization density at the S(1) site compared to the magnetization density plots of stoichiometric, C(1) and N(1) doped GFO.

The O *p*-electrons generating the inner and outer polarization in stoichiometric GFO (Fig. 3(a)) exhibit less energetic separation. They are almost evenly distributed along the energy range of −5 eV up to −1 eV. This is in contrast to the C(1)/C(2) and N(1)/N(2) doped case where the covalent bond between the anion and Fe atoms is formed in the energy range of −1 eV up to the Fermi level.

The calculated AFM coupling strength of stoichiometric GFO is 1.54 eV. Even though the simulation cell's geometry is altered introducing the S(1) atom the effect on the overall AFM coupling strength is small being reduced by only 60 meV (see Table 4).

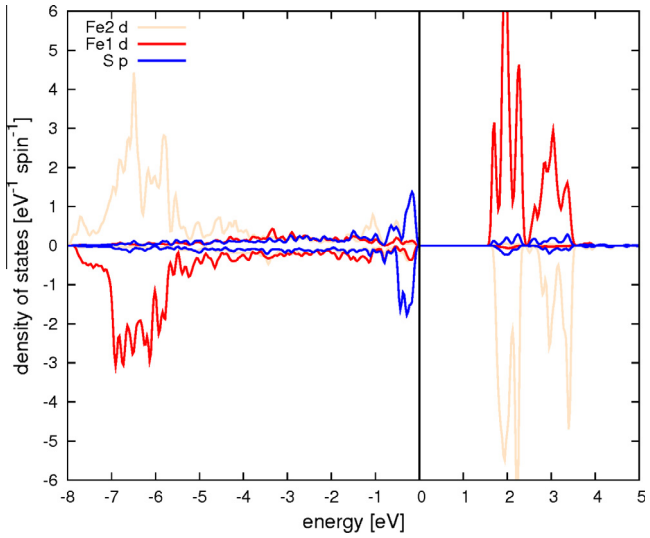

Fig. 8. PDOS of the Fe1$_a$–S(1)–Fe2 configuration in GFOS(1). Given in red and beige are the Fe1$_a$ and Fe2 *d*-states. Highlighted in blue are the S *p*-states. (For interpretation of the references to color in this figure legend, the reader is referred to the web version of this article.)

4.3.2. S(2) substitution

Exchanging O(2) by a S atom has similar effects on the GFO simulation cell. The band gap reduces by more than 1 eV and the cell volume enhances by 6.5%. Both Fe–S(1) bond lengths of the Fe1$_b$–S(2)–Fe2 configuration increase compared to the undoped system. The Fe1$_b$–S(2)–Fe2 enclosed angle decreases to 119.35° and the AFM coupling strength is reduced to −1.45 eV.

4.3.3. S(3) substitution

Cell site substitution (3) shows an AFM coupling strength of only −0.44 meV. The structure of the AFM coupling strength mediating Fe1–O–Fe2 chains are distorted in a way that the respective Fe–O orbital overlap reduces. As a consequence the respective doping configuration becomes the energetically most unfavorable one. The band gap is slightly enhanced compared to the S(1) and S(2) substitution. The Fe1$_b$–S(3)–Fe2 enclosed angle is increased to 106.40°.

4.3.4. S(4) substitution

In the S(4) substitution case the AFM coupling strength differs only by 30 meV compared to stoichiometric GFO. The band gap is reduced the least and the distance to the Fe2 atom is increased by +10.3%. Since the AFM coupling strength is similar to stoichiometric GFO one can assume that the Fe1–O–Fe2 chains

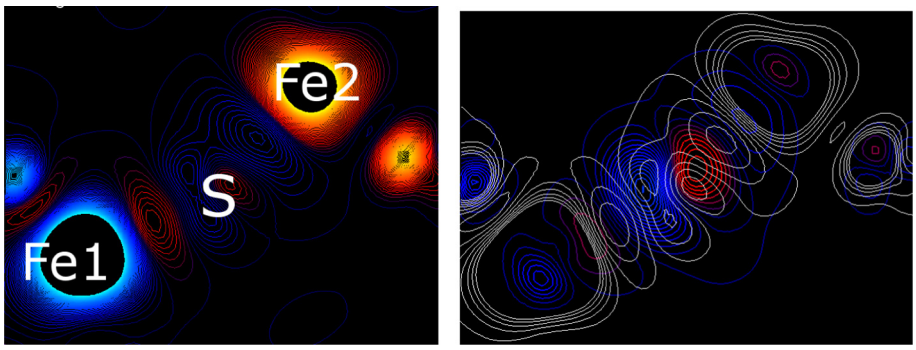

Fig. 9. Magnetization density of the $Fe1_a$–S(1)–Fe2 complex in GFOS(1). Given in red and blue are positive and negative spin densities, respectively. (a) Shows the spin density of all occupied states. (b) Gives the partial spin density in the energy range of −1 eV up to the Fermi level. (For interpretation of the references to color in this figure legend, the reader is referred to the web version of this article.)

exhibit almost no structural distortions in this doping configuration.

5. Discussion

Our calculations show that exchanging O with a C, N or S atom, changes the electronic and magnetic properties of GFO in several quite different ways. Of all investigated doping configurations (1)–(4) cell site substitution (1) is the energetically most stable substitution site for the C, N and S impurity atom.

Substituting O with C yields an either ferrimagnetic or antiferromagnetic ground state. Carbon placed on sites (1) and (2) introduces a ferrimagnetic ground state and ferrimagnetic coupling in the respective Fe1–C(1/2)–Fe2 configuration. The C(1) and the C (2) atoms form an additional covalent bond with the corresponding next nearest Fe2 atom and reduce its magnetic moment from $4\mu_B$ to $3\mu_B$ compared to the Fe1 atom and results in a ferrimagnetic exchange. Carbon itself carries a magnetic moment of about half a μ_B on cell sites (1), (2) and (4) which is antiparallel to the magnetic moment of its next nearest Fe2 atom due to the enhanced interaction. C(3) is non magnetic and yields an AFM ground state in GFOC (3). The C(3) atom is part of the AFM superexchange weak mediating Fe1–C(3)–Fe2 complex.

Regarding the calculated band gaps of the different C doping configurations with respect to the photocatalytic properties C doping shows a band gap reduction for all doping configurations. Cell site substitution (1), (2), (4) yield a magnetic ground state of $-2\mu_B$ per simulation cell yielding unequal spin up and spin down gaps. In the C(1), C(2) and C(4) doped case spin up acceptor states are introduced near the CB (conduction band), leading to a reduced majority spin gap. The spin gap is reduced the most for the cell site (3) substitution for about more than 1 eV compared to stoichiometric GFO to about 1.40 eV for both spin channels. The C(3) substitution case, however, exhibits impurity states that are not attached to the CB, but located near the mid band gap energy.

Impurity states located in the middle of the band gap between the VB and CB are known to act as recombination centers reducing the electron-hole life time decreasing the photocatalytic efficiency. To create a good photocatalyst one desires a "clean" band gap with no additional states. Doping GFO with C, N and S regarding the application as a photocatalyst should narrow the band gap without introducing mid-band gap states minimizing the recombination rate of the charge carriers [39,40]. This, however, is fulfilled for the C(1), C(2) and C(4) doping configurations with impurity acceptor states that are either attached or near the CB.

Substituting O with N introduces a ferrimagnetic ground state with a total magnetic moment of $-1\mu_B$ per simulation cell for all investigated doping configurations N(1–4). Nitrogen indeed mediates the AFM coupling inside the Fe1–N(1/2)–Fe2 bonds but does not induce a ferrimagnetic coupling as C(1) and C(2) in the Fe1–C (1/2)–Fe2 configurations. The N atom, however, carries a magnetic moment yielding the non zero magnetic ground state of GFON.

Comparing the structural parameters of the doped Fe1–X–Fe2 bonds inside the respective GFOX simulation cell, C induces larger distortions in the atomic bonds and angles than N. Regarding the structure of the band gaps, N introduces acceptor states in the spin up channel near the mid-band gap. This, however, indicates an enhanced interaction with the neighboring Fe2 atom, also represented by the reduced Fe2–N bond length. All N doping configurations show a reduction of both the spin up and spin down gap, which is more pronounced for the spin up case due to acceptor states.

Dhanasekaran and Gupta [19], however, report increased water splitting properties incorporating N impurities to GFO. Despite the acceptor state located in the spin up channel the spin down channel shows no impurity states and is reduced as well compared to stoichiometric GFO. Our results therefore support the measured enhanced photocatalytic property of N doped GFO.

Exchanging O with S yields an AFM ground state for all doping configurations (1)–(4). The magnetic exchange mechanism mediated via the S atom is similar to the O atom. S, however, introduces notably changes in the cell geometry due to its large atomic radius. Even though the Fe1–S–Fe2 bond lengths are enhanced compared to the undoped case the partial bond length ratio (Fe1–X to Fe2–X) are similar. This is in contrast to the C(1/2) and N(1/2) doping configurations where C and N show decreased and increased Fe2–X and Fe1–X bond lengths, respectively, compared to stoichiometric GFO.

The S(1) and S(2) doping configuration shows the highest band gap reduction and are energetically more favorable than the S(3) and S(4) substitution. The respective band gaps are free of doping states supporting the experimentally measured enhanced photocatalytic property of GFOS compared to stoichiometric GFO [19].

Regarding the AFM coupling strengths there is a highly reduced energy difference between the AFM ground state and a hypothetic FM state for doping configuration S(3). This, however, can be explained by the distinct distortion the two Fe clusters that mediate the AFM superexchange throughout the crystal. Experiments [13] on Mn doped GFO report reduced Curie temperatures, which the authors try to explain either by a weakened AFM coupling of the Mn–O–Fe bonds or distorted Fe–Fe linkages and angles reducing the AFM superexchange. In the light of our results we will also expect a reduction of the Curie temperature upon doping with S.

6. Conclusion

We investigate the effect of single anion substitution in GFO, exchanging O by a C, N and S atom. In total we examined four different substitution sites for each dopant. Concluding our results we indeed see changes in magnetic and electronic properties and report substitution site dependent behavior. The performed calculations support the experimentally measured enhanced photocatalytic properties of N and S doped GFO. Further, we find AFM and ferrimagnetic ground states in C doped GFO, depending on the respective doping site. Large structural distortions evoked by the incorporation of S are suspected to decrease the Curie temperature and to affect the polarization inside GFOS due to highly distorted O octahedra. Doping GFO with C, N, and S exhibit properties interesting for future technical applications. Using *ab initio* DFT calculations as a predictive tool we hope to encourage future experiments and may support their interpretation.

Acknowledgements

The authors acknowledge support from the Austrian Science Fund FWF within SFB ViCoM F4109-N28 P09. For visualizing the respective geometries and acquired data we used the VESTA [41] and VisIt [42] packages.

Appendix A. Supplementary material

Supplementary data associated with this article can be found, in the online version, at http://dx.doi.org/10.1016/j.commatsci.2016.02.017.

References

[1] Nicola A. Spaldin, Manfred Fiebig, Science 309 (2005) 391–392.
[2] Sang-Wook Cheong, Maxim Mostovoy, Nat. Mater. 6 (1) (2007) 13–20.
[3] R. Ramesh, Nicola A. Spaldin, Nat. Mater. 6 (1) (2007) 21–29.
[4] T. Arima, D. Higashiyama, Y. Kaneko, J. He, T. Goto, S. Miyasaka, T. Kimura, K. Oikawa, T. Kamiyama, R. Kumai, Y. Tokura, Phys. Rev. B 70 (6) (2004) 064426 (August).
[5] Yu. F. Popov, A.M. Kadomtseva, G.P. Vorobev, V.A. Timofeeva, D.M. Ustinin, A.K. Zvezdin, M.M. Tegeranchi, J. Exp. Theor. Phys. 87 (1) (1998) 146–151.
[6] Somdutta Mukherjee, Amritendu Roy, Sushil Auluck, Rajendra Prasad, Rajeev Gupta, Ashish Garg, Phys. Rev. Lett. 111 (8) (2013) 087601 (August).
[7] J.P. Remeika, J. Appl. Phys. 31 (5) (1960) S263–S264.
[8] Christophe Lefevre, Francois Roulland, Alexandre Thomasson, Christian Meny, Florence Porcher, Gilles André, Nathalie Viart, J. Phys. Chem. C 117 (28) (2013) 14832–14839.
[9] V. Raghavendra Reddy, Kavita Sharma, Ajay Gupta, A. Banerjee, J. Magn. Magn. Mater. 362 (0) (2014) 97–103.
[10] Alexandre Thomasson, Fatima Ibrahim, Christophe Lefevre, Emmanuel Autissier, François Roulland, Christian Mény, Cédric Leuvrey, Sukgeun Choi, William Jo, Olivier Crégut, Gilles Versini, Sophie Barre, Mébarek Alouani, Nathalie Viart, RSC Adv. 3 (9) (2013) 3124.
[11] M. Venkatesan, C.B. Fitzgerald, J.G. Lunney, J.M.D. Coey, Phys. Rev. Lett. 93 (17) (2004) 177206.
[12] Chan-Ho Yang, Daisuke Kan, Ichiro Takeuchi, Valanoor Nagarajan, Jan Seidel, Phys. Chem. Chem. Phys. 14 (2012) 15953–15962.
[13] M. Bakr Mohamed, H. Fuess, J. Magn. Magn. Mater. 323 (15) (2011) 2090–2094.
[14] Rana Saha, Ajmala Shireen, Sharmila N. Shirodkar, Umesh V. Waghmare, A. Sundaresan, C.N.R. Rao, J. Solid State Chem. 184 (9) (2011) 2353–2359.
[15] T.C. Han, Y.C. Lee, Y.T. Chu, Appl. Phys. Lett. 19 (12) (2014) 19995–20022.
[16] Xu Qing-Yu, Wen Zheng, Gao Jin-Long, Wu Di, Qiu Teng, Tang Shao-Long, Xu Ming-Xiang, Chin. Phys. B 20 (8) (2011) 087505.
[17] Y.C. Hu, Z.Z. Jiang, K.G. Gao, G.F. Cheng, J.J. Ge, X.M. Lv, X.S. Wu, Chem. Phys. Lett. 534 (2012) 62–66.
[18] Pushkar Kanhere, Zhong Chen, Molecules 19 (12) (2014) 212407.
[19] P. Dhanasekaran, N.M. Gupta, Int. J. Hydrogen Energy 37 (6) (2012) 4897–4907 (March).
[20] J. Atanelov, P. Mohn, Phys. Rev. B 92 (10) (2015) 104408.
[21] G. Kresse, J. Hafner, Phys. Rev. B 47 (January) (1993) 558–561.
[22] G. Kresse, J. Hafner, Phys. Rev. B 49 (May) (1994) 14251–14269.
[23] G. Kresse, J. Hafner, J. Phys.: Condens. Matter 6 (40) (1994) 8245.
[24] G. Kresse, J. Furthmüller, Comput. Mater. Sci. 6 (1) (1996) 15–50.
[25] G. Kresse, J. Furthmüller, Phys. Rev. B 54 (October) (1996) 11169–11186.
[26] G. Kresse, D. Joubert, Phys. Rev. B 59 (January) (1999) 1758–1775.
[27] P.E. Blöchl, Phys. Rev. B 50 (December) (1994) 17953–17979.
[28] S.L. Dudarev, G.A. Botton, S.Y. Savrasov, C.J. Humphreys, A.P. Sutton, Phys. Rev. B 57 (January) (1998) 1505–1509.
[29] Jochen Heyd, Gustavo E. Scuseria, Matthias Ernzerhof, J. Chem. Phys. 118 (18) (2003) 8207–8215.
[30] Jochen Heyd, Gustavo E. Scuseria, J. Chem. Phys. 121 (3) (2004) 1187–1192.
[31] Jochen Heyd, Gustavo E. Scuseria, Matthias Ernzerhof, J. Chem. Phys. 124 (21) (2006).
[32] Aliaksandr V. Krukau, Oleg A. Vydrov, Artur F. Izmaylov, Gustavo E. Scuseria, J. Chem. Phys. 125 (22) (2006).
[33] Fumiyasu Oba, Atsushi Togo, Isao Tanaka, Joachim Paier, Georg Kresse, Phys. Rev. B 77 (24) (2008) 245202 (1959).
[34] S.J. Clark, J. Robertson, S. Lany, A. Zunger, Phys. Rev. B 81 (11) (2010) 115311 (1959).
[35] Chris G. Van de Walle, Anderson Janotti, Phys. Status Solidi (B) 248 (1) (2011) 19–27 (1959).
[36] M. Hatnean, J. Robert, M.T. Fernandez Diaz, E. Ressouche, A. Cousson, L. Pinsard-Gaudart, S. Petit, Eur. Phys. J. Spec. Top. 213 (1) (2012) 69–76 (December).
[37] F. Ibrahim, M. Alouani, Phys. Rev. B 85 (17) (2012) 174411 (May).
[38] N. Wang, F.S. Wen, L. Li, Y.F. Lü, S.C. Liu, Y.F. Lu, Z.Y. Liu, B. Xu, J.L. He, D.L. Yu, Y. J. Tian, J. Magn. Magn. Mater. 322 (21) (2010) 3595–3600.
[39] W. Shockley, W.T. Read Jr., Phys. Rev. 87 (5) (1952) 835.
[40] R.N. Hall, Phys. Rev. 87 (2) (1952) 387.
[41] Koichi Momma, Fujio Izumi, J. Appl. Crystallogr. 44 (6) (2011) 1272–1276.
[42] H. Childs, E. Brugger, B. Whitlock, J. Meredith, S. Ahern, D. Pugmire, K. Biagas, M. Miller, C. Harrison, G.H. Weber, H. Krishnan, T. Fogal, A. Sanderson, C. Garth, E.W. Bethel, D. Camp, O. Rübel, M. Durant, J.M. Favre, P. Navrátil, VisIt: an end-user tool for visualizing and analyzing very large data, in: High Performance Visualization – Enabling Extreme-Scale Scientific Insight, 2012, pp. 357–372.